

Non-destructive evaluation of freeze-thaw performance in ISS-lime-fly ash stabilized saline soils

Jiyun Nan ^{a,b}, Jiankun Liu ^{b,c}, Dan Chang ^b, Jong-Sub Lee ^{a,*}, Xue Li ^{d,**}

^a School of Civil, Environmental and Architectural Engineering, Korea University, 145, Anamro, Seongbuk-gu, Seoul, 02841, Republic of Korea

^b School of Civil Engineering, Sun Yat-sen University, Guangzhou, 510275, China

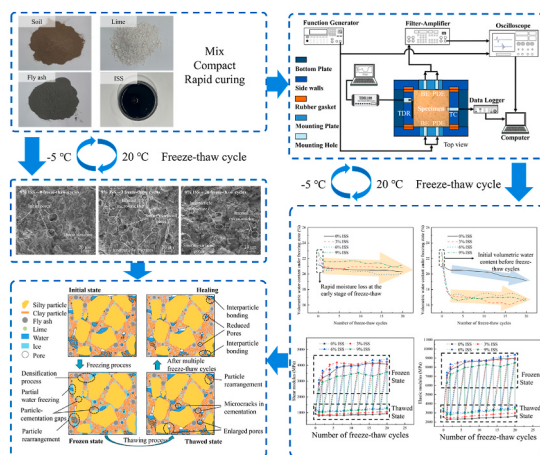
^c Southern Marine Science and Engineering Guangdong Laboratory, Zhuhai, 519082, China

^d State Key Laboratory of Internet of Things for Smart City and Department of Civil and Environmental Engineering, University of Macau, Macao SAR, China

HIGHLIGHTS

- ISS-lime-fly ash system improves freeze-thaw durability of saline soils.
- NDT techniques monitor strength and moisture in real time.
- ISS enhances bonding and reduces unfrozen water content.
- Approach lowers carbon emissions vs. cement-based methods.

GRAPHICAL ABSTRACT



ARTICLE INFO

Keywords:
Sustainable soil stabilization
Saline soil
Freeze-thaw resistance
Ionic soil stabilizer
Non-destructive testing

ABSTRACT

Replacing conventional cement-based binders with cleaner materials for soil stabilization has become a research priority due to the pressing need to reduce carbon emissions in the construction sector. This study explores a sustainable stabilization method using ionic soil stabilizer (ISS), lime, and fly ash to improve the freeze-thaw durability of saline soils, which pose serious challenges to infrastructure in cold regions. A series of non-destructive testing methods, including elastic wave velocity measurements (S-wave and P-wave), time-domain reflectometry for volumetric water content analysis, and scanning electron microscopy, were employed to assess soil stabilization efficiency. The results indicate that ISS-lime-fly ash stabilization significantly enhances the freeze-thaw resistance of saline soils by promoting aggregate formation, improving cementitious bonding, and reducing the temperature sensitivity of water content in the frozen state. The evolution of S-wave and P-wave velocities revealed that ISS-lime-fly ash treated specimens exhibited greater structural integrity and slower

* Corresponding author.

** Corresponding author.

E-mail address: jongsuh@korea.ac.kr (J.-S. Lee).

degradation in mechanical properties compared to lime-fly ash treated soils. After 20 freeze-thaw cycles, the thawed ISS-lime-fly ash stabilized soils exhibited shear modulus values ranging from 1055 to 1325 MPa and small-strain Young's modulus values from 2973 to 3644 MPa. Integrating microstructural observations with existing research, this study elucidates freeze-thaw damage and self-healing mechanisms in stabilized soils while revealing the influence of ISS content on freeze-thaw behavior. These findings support the development of low-carbon soil materials for sustainable construction in cold and saline regions.

1. Introduction

In large-scale infrastructure projects such as roads and bridges, the use of problematic natural soils often results in structural degradation and frequent maintenance. These recurring interventions not only entail excessive resource consumption but also contribute to elevated carbon emissions and increased construction waste, thereby exacerbating environmental burdens. In cold regions, subgrade soils are subjected to cyclic freeze-thaw processes that markedly deteriorate their mechanical properties. Saline soils, in particular, are highly susceptible to frost heave, settlement, and moisture migration, leading to structural failures such as pavement cracking, subsidence, and erosion (Chen et al., 2023; Dong et al., 2024; Wan et al., 2017; Zhang et al., 2024, 2020; X. Zhang et al., 2023). Therefore, developing effective stabilization methods to improve the freeze-thaw durability of saline soils is crucial for enhancing infrastructure resilience and promoting sustainable development in cold regions.

To enhance the engineering properties of problematic soils, inorganic stabilizers, particularly lime, cement, and fly ash, have been widely adopted (Chen et al., 2022; Le Runigo et al., 2009; Liu et al., 2019; Niu et al., 2024; Stipro, 1989; Sun et al., 2023; F. Wang et al., 2022; Zha et al., 2008). These stabilizers effectively increase soil strength, reduce moisture sensitivity, and improve frost resistance, making them essential for foundation and pavement applications. In cold regions, inorganic stabilizers remain the primary approach for treating saline soil. For instance, lime-based stabilization requires optimization to balance cation exchange and plasticity changes. Excessive lime content may diminish plasticity and coarsen soil particles after freeze-thaw cycles, resulting in larger pores and reduced UCS (Liu et al., 2019). The combination of lime and fly ash has been shown to effectively mitigate strength deterioration caused by freeze-thaw cycles. As a complementary stabilizer, fly ash plays a crucial role in reducing salt-induced expansion and reinforcing soil structure, ultimately improving the durability and stability of treated soils (Chen et al., 2022). Additionally, fly ash has been reported to alleviate the negative effects of freeze-thaw cycles on soil wet aggregate stability, bulk density, and permeability (Sahin et al., 2008).

In the pursuit of sustainable construction, replacing traditional cement-based binders with lower-carbon and more sustainable alternatives has become a pressing concern, particularly for ground improvement. The production of cement and lime is highly energy-intensive and represents a major source of greenhouse gas (CO_2) and acidifying (SO_2) emissions (Amin et al., 2023; Cabeza et al., 2013; Qaidi et al., 2022). As a result, the use of industrial by-products and novel alternatives like ionic soil stabilizers (ISS) is gaining momentum as strategies to mitigate environmental footprints and advance cleaner construction practices (Kakasor Ismael Jaf et al., 2023; Pourakbar et al., 2024; Yan et al., 2024a).

ISS represents a class of non-traditional chemical additives that offer environmental advantages over conventional stabilizers. For instance, replacing 12 tons of lime with 5 gallons of a concentrated additive can reduce CO_2 emissions by over 15 tons and save energy equivalent to 2000 kWh (RoadbondInc., 2010). These additives have also shown effectiveness in improving compaction characteristics, shear strength, and reduction of soil expansiveness (Al-Dakheeli et al., 2021; Wu et al., 2021a). It is a liquid reagent that diffuses easily within soil matrices, facilitating complex physical and chemical interactions. At the

microscopic level, ISS alters the surface properties of clay minerals, reducing their water affinity. This effect is achieved through mechanisms such as interlayer cation exchange, mineral encapsulation, and the removal of interlayer water (Al-Dakheeli et al., 2021; Lei et al., 2023). With these advantages, ISS-stabilized soil maintains higher strength than untreated soil (X. Wang et al., 2022). When integrated with inorganic stabilizers, ISS can further augment soil stabilization efficacy. For example, the incorporation of ISS with cement and activated carbon markedly enhances soil densification while mitigating contaminant leaching (Ma et al., 2018). In recent years, ISS has also been investigated for its potential in stabilizing cold-region soils. When applied to red clay, ISS-stabilized soil exhibits higher strength than untreated soil after freeze-thaw cycles (X. Wang et al., 2022). However, when used in expansive soils, ISS-treated specimens have been found to exhibit lower shear strength than their untreated counterparts (Wang et al., 2018). Jia et al. (2024) demonstrated that incorporating ISS with lime and fly ash enhances cementitious reactions while reducing the adsorbed water layer thickness, leading to improved freeze-thaw resistance and mechanical performance. Additionally, Yan et al. (2024a) found that ISS significantly enhances the mechanical performance of lime-fly ash stabilized saline soil under freezing conditions. However, despite these advancements, the stabilization behavior and freeze-thaw resistance of saline soil treated with ISS and inorganic materials remain insufficiently understood.

To accurately assess the stabilization effectiveness of saline soils during freeze-thaw cycles, it is essential to employ appropriate testing methods that capture soil behavior dynamically. Traditional destructive tests require the preparation of new specimens for each freeze-thaw stage, resulting in fragmented datasets, high material consumption, and increased environmental impacts during the testing process. In contrast, non-destructive testing provides an effective approach for evaluating material integrity by detecting surface and internal defects, without compromising the structure or functionality of material (Dwivedi et al., 2018; Kumar and Mahto, 2013; Wei et al., 2024). In laboratory investigations, methods such as bender elements, piezo disk elements, and time-domain reflectometry (TDR) offer significant advantages for studies requiring repeated or process-oriented observations, as they do not damage specimens. Furthermore, these techniques enable real-time monitoring of shear wave (S-wave) velocity, compressional wave (P-wave) velocity, and volumetric water content throughout testing (Davis and Chudobiak, 1975; Lee et al., 2020a; Leong et al., 2005; Park et al., 2021; Xu et al., 2022). This capability is particularly crucial for soils during freeze-thaw cycling. This approach effectively captures the dynamic interactions between frozen and unfrozen water, providing valuable insights into soil freezing behavior and strength evolution.

Despite increasing attention to sustainable soil stabilization and the use of low-carbon materials, the synergistic effects of combining traditional inorganic agents with ISS in saline soils, particularly under cyclic freeze-thaw conditions in cold regions, remain insufficiently investigated. Furthermore, a continuous and in-depth understanding of the mechanical behavior and underlying mechanisms of ISS and inorganic-stabilized saline soils during freeze-thaw cycles is still lacking. This study addresses this gap by combining ISS with lime and industrial by-product fly ash to enhance soil stabilization. Advanced non-destructive testing techniques such as bender elements, piezo disk elements, and TDR were used to monitor changes in mechanical properties

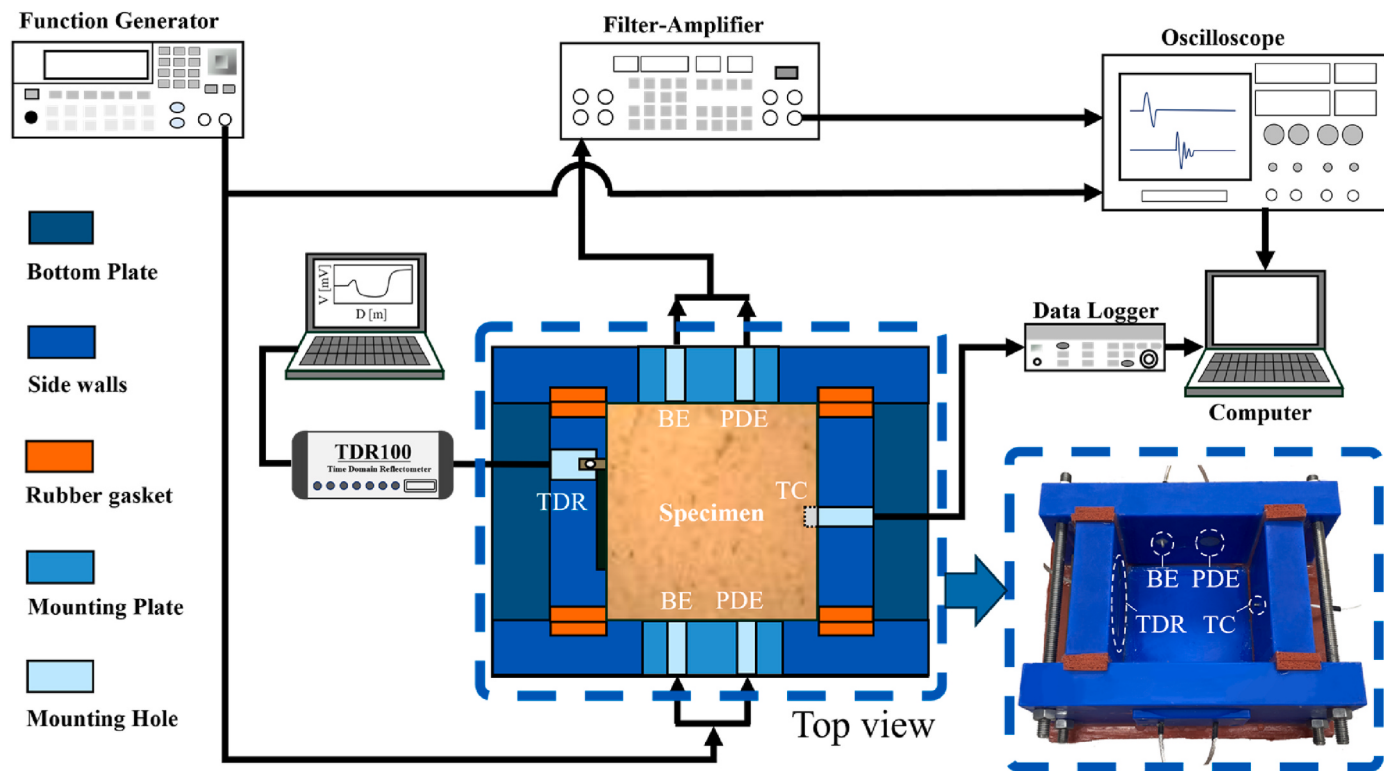


Fig. 1. Equipment diagram.

and unfrozen water content throughout the freeze-thaw cycles. In addition, scanning electron microscopy was used to investigate the microstructural evolution of stabilized specimens during freeze-thaw cycles.

2. Materials and methods

2.1. Materials

The saline soil used in this research was collected from the NCE8# road construction site in the southern area of Lanzhou New District, Yongdeng County, Lanzhou City, Gansu Province, China. The sampling location is clearly illustrated in Fig. S1. It is a natural silty clay with a salinity level of 0.56 %. Table S1 presents the primary anions and cations determined through Ion Chromatography (DX-600) and Inductively Coupled Plasma Emission Spectroscopy (iCAP Qc). Based on the *PRC National Standard (GB50021-2001)* for geotechnical engineering investigation, this soil is classified as medium and sulfurous saline soil. Table S2 summarizes the basic physical properties, while the grain size distribution curve is depicted in Fig. S1. According to the geotechnical test code of the *Unified Soil Classification System (USCS)*, the soil sample is classified as silty clay (CL).

A quicklime with a CaO content of 75–80 % was selected as the additive. The composition and loss on ignition of fly ash are provided in Table S3. Both the quicklime and fly ash were sourced from Gongyi Yuanheng Water Purification Material Factory. The ionic soil stabilizer (ISS) used in this study was Roadbond EN-1, a product of Roadbond Service Company (Fig. S1). This stabilizer is a black chemical concentrate that requires dilution with water prior to use. Its main component is D-limonene (citrus stripper oil), a citrus-derived byproduct commonly used as a solvent or intermediate in organic synthesis within the chemical industry. Roadbond EN-1 exhibits properties similar to concentrated sulfuric acid (Scholen, 1992), with a sulfate concentration above 1 %, surface-active agent mass fraction of 6 %, sulfur content of 1 mg/m³, density of 1.709 g/cm³, and pH of 1.05. When treated with

sulfuric acid, it forms a mildly corrosive solution that becomes environmentally benign after dilution.

2.2. Equipment and sample preparation

2.2.1. Equipment

Four custom-designed nylon cells were developed to prepare stabilized soil specimens and measure P-wave velocity, S-wave velocity, volumetric water content, and temperature. As shown in Fig. 1, each cell consists of four nylon side walls and a bottom plate, with internal dimensions of 10 cm × 10 cm × 8 cm. The dimensions were designed with reference to previous studies by Park et al. and Kang et al. (Kang and Lee, 2015; Park and Kim, 2023). A pair of bender elements and piezo disk elements are mounted on the front and rear plates, respectively. Three parallel L-shaped TDR probes, each 50 mm in length and spaced 5 mm apart, are installed at the center of the left plate. The probes are connected to a TDR reflectometer (Hyperlabs Inc, HL1101 Ruggedized USB TDR) via a coaxial cable, with the inner conductor linked to the central probe and the outer conductor split to connect the two outer probes (Kim et al., 2021). Electromagnetic wave signals from the TDR probes are recorded by the TDR reflectometer and stored digitally. A temperature sensor is positioned at the center of the right plate. The temperature sensor is connected to a data logger (Agilent Technologies, Model 34972A LXI Data Acquisition/Switch Unit), enabling real-time data acquisition and storage via a computer. During wave velocity measurement, signals are generated by a function generator (Keysight Technologies, Model 33500B Series), transmitted from the transmitter to the receiver, and processed through a filter amplifier (Krohn-Hite Corporation, Model 3944) for signal enhancement and noise reduction. The processed signals are displayed on an oscilloscope (Agilent Technologies, Model DSO-X 3014A InfiniiVision) and saved for further analysis. During freeze-thaw cycles, all four cells were placed in an incubator, with cables from the sensors passing through small openings in the incubator to connect with external devices, ensuring continuous data acquisition under controlled environmental conditions.

2.2.2. Sample preparation

Previous studies have demonstrated that soil stabilized with 6 % quicklime exhibits superior performance (Nan et al., 2022), leading to the selection of 6 % quicklime by dry soil weight for this study. Similarly, the fly ash content was set at 15 % by dry soil weight based on prior research findings (Karami et al., 2021). The ISS was diluted with water at a 1:150 vol ratio before mixing. To evaluate the effects of ISS on stabilized soils, diluted ISS solution was added at dosages equivalent to 3 %, 6 %, and 9 % of the dry soil mass, with the remaining moisture supplied by distilled water. The specimens were labeled as 3 % ISS, 6 % ISS, and 9 % ISS accordingly. A control specimen containing only 6 % quicklime and 15 % fly ash was labeled as 0 % ISS. The optimum moisture contents for 0 % ISS, 3 % ISS, 6 % ISS, and 9 % ISS specimens were determined to be 18.95 %, 20.50 %, 19.22 %, and 16.90 %, respectively, while their maximum dry densities were measured as 1.64 g/cm³, 1.63 g/cm³, 1.65 g/cm³, and 1.67 g/cm³, respectively.

Untreated soil was initially mixed with 6 % quicklime and 15 % fly ash, with water added first, followed by ISS solutions, to achieve a total water content of 19 %, which included the water from the ISS. The ISS solutions were introduced in increments of 3 %, 6 %, and 9 % by weight, with each addition divided into two stages and a 15-min interval to enhance interaction between the stabilizer and the mixture. After the second addition, specimens were sealed and left undisturbed for 24 h to ensure uniform moisture distribution. To ensure consistent conditions across different ISS contents, the density of all specimens was controlled at 1.57 g/cm³, corresponding to 95 % of the average maximum dry density. The mixtures were compacted into nylon cells and sealed after compaction.

Following compaction, the specimens were sealed and cured at 60 °C to accelerate the experimental process, in accordance with the *Test Methods of Materials Stabilized with Inorganic Binders for Highway Engineering*. Based on the authors' previous findings, curing at 60 °C for 24 h is equivalent to curing at 20 °C for 28 days (Nan et al., 2025). To study the impact of freeze-thaw cycles, the cured specimens were placed in a temperature-controlled incubator. Each freeze-thaw cycle involved freezing at -5 °C for 12 h, ensuring complete frost penetration, followed by thawing at 20 °C for 12 h. A total of 20 freeze-thaw cycles were performed. During the 1st, 2nd, 4th, 6th, 8th, 10th, 12th, 14th, 16th, 18th, and 20th cycles, P-wave velocity, S-wave velocity, volumetric water content, and temperature data were recorded during both the freezing and thawing phases. These measurements were used to assess the effects of freeze-thaw cycles on wave velocities and volumetric water content.

To observe the microstructural changes of specimens during the freeze-thaw process, samples were collected before freezing, after three cycles, and after twenty cycles. Each specimen was cut into blocks measuring 1 cm × 0.5 cm × 0.5 cm, freeze-dried, and then fractured at the center to expose an undisturbed surface for scanning electron microscopy analysis (Nan et al., 2024).

2.3. Calibration

The temperature sensor (TP100) and TDR probe were calibrated before the main experiment. For temperature sensor calibration, pure water at approximately 50 °C was placed in the cell, and its temperature was gradually decreased to around 5 °C. During this process, the water temperature and the corresponding resistance values of the sensor were recorded using a thermometer and an LCR meter at intervals of approximately 5 °C. The TP100 thermistor was calibrated based on its linear relationship with temperature. Following calibration, the measured specimen temperatures during the freezing phase are shown in Fig. S2. Results confirm that the specimens fully froze to -5 °C during the freezing phase and completely thawed to 20 °C during the melting phase.

To account for the potential influences of the nylon specimen cell and soil on the electromagnetic properties of the TDR probe, calibration tests

were conducted before the experiments to establish the correlation between volumetric water content and relative permittivity (Hong et al., 2016; Kim et al., 2021; Lee et al., 2020b). The propagation time of electromagnetic waves in the soil-filled specimen cell is governed by the relative permittivity of soil, as described by the following equation (Baker and Allmaras, 1990; Noborio, 2001):

$$\varepsilon_r = \left(\frac{c}{v}\right)^2 = \left(\frac{c \times \Delta t}{2L}\right)^2 = \left(\frac{L_a}{L}\right)^2 \quad (1)$$

where ε_r represents the relative permittivity; c and v are the speed of electromagnetic waves in a vacuum and in the measured soil, respectively; Δt and L represent the propagation time of electromagnetic waves in the soil specimen and the length of the TDR probe, respectively. $L_a = \frac{c \times \Delta t}{2}$ is the apparent probe length, representing the effective distance between the start and end points of the wave reflection along the probe.

The stabilizers and soil were thoroughly mixed according to the designated stabilizer dosage ratios. Subsequently, a sufficient amount of water was added to achieve volumetric water contents of 10 %, 15 %, 20 %, 25 %, 30 %, and 35 %, respectively. The specimens were then compacted in five layers to the designed dry density according to the designed value of 1.57 g/cm³. Immediately after compaction, the TDR device was used to collect electromagnetic wave signals, which were then saved to a computer. The second reflection point is determined by the intersection of the two tangents (Noborio, 2001), as shown in Fig. S3 (a). After obtaining the apparent probe length (L_a), the relative permittivity of the specimen was calculated using Eq. (1). Then, based on calibration using data at different volumetric water content levels, the relationship between volumetric water content and relative permittivity can be expressed by the cubic polynomial Eq (Topp et al., 1980), as follows:

$$\theta_v = a \cdot \varepsilon_r^3 - b \cdot \varepsilon_r^2 + c \cdot \varepsilon_r - d \quad (2)$$

where θ_v represents the volumetric water content; ε_r represents the relative permittivity; a , b , c , d represent the fitting parameters. Relative Eqs. of specimens are all shown in Fig. S3 (b).

2.4. Wave velocity measurement and elastic modulus calculation

The S-wave and P-wave signals were recorded during selected freeze-thaw cycles as described in the previous section. The first arrival time of the S-wave signals was determined using the zero after first bump method (Lee and Santamarina, 2005). For P-waves, the arrival time was identified as the point where the waveform amplitude begins to rise noticeably above the background noise, marking the onset of seismic oscillations, commonly referred to as the first break (Linneman et al., 2021). The elastic wave velocities were calculated using the following equation:

$$V = L / \Delta t \quad (3)$$

where V represents the wave velocity, L is the distance between sensors, Δt is the travel time.

Based on previous research, the shear modulus and elastic modulus of the specimens can be derived from S- and P-wave velocities using the following equations (Vinson, 1978; Zhang et al., 2018):

$$E_0 = \frac{\rho V_s^2 (3V_p^2 - 4V_s^2)}{V_p^2 - V_s^2} \quad (4)$$

$$G_0 = \rho V_s^2 \quad (5)$$

where G_0 and E_0 represent the shear modulus and small-strain Young's modulus, respectively, while V_p , V_s , and ρ denote the P-wave velocity, S-wave velocity, and mass density under small-strain conditions.

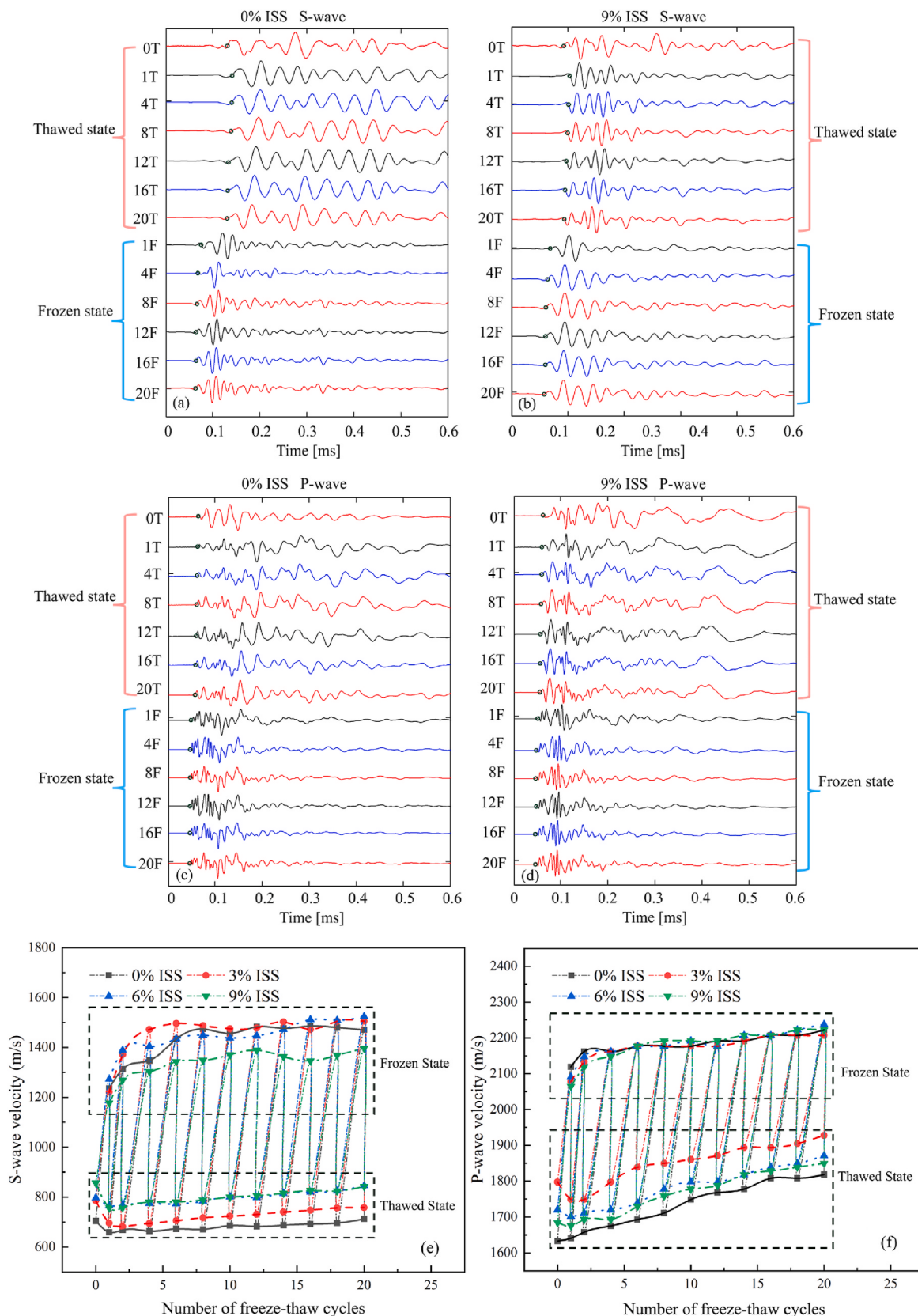


Fig. 2. Elastic wave signals and wave velocity results of specimens with different ISS contents: (a) S-wave signals of the 0 % ISS specimen; (b) S-wave signals of the 9 % ISS specimen; (c) P-wave signals of the 0 % ISS specimen; (d) P-wave signals of the 9 % ISS specimen; (e) S-wave velocities of specimens with varying ISS contents; (f) P-wave velocities of specimens with varying ISS contents.

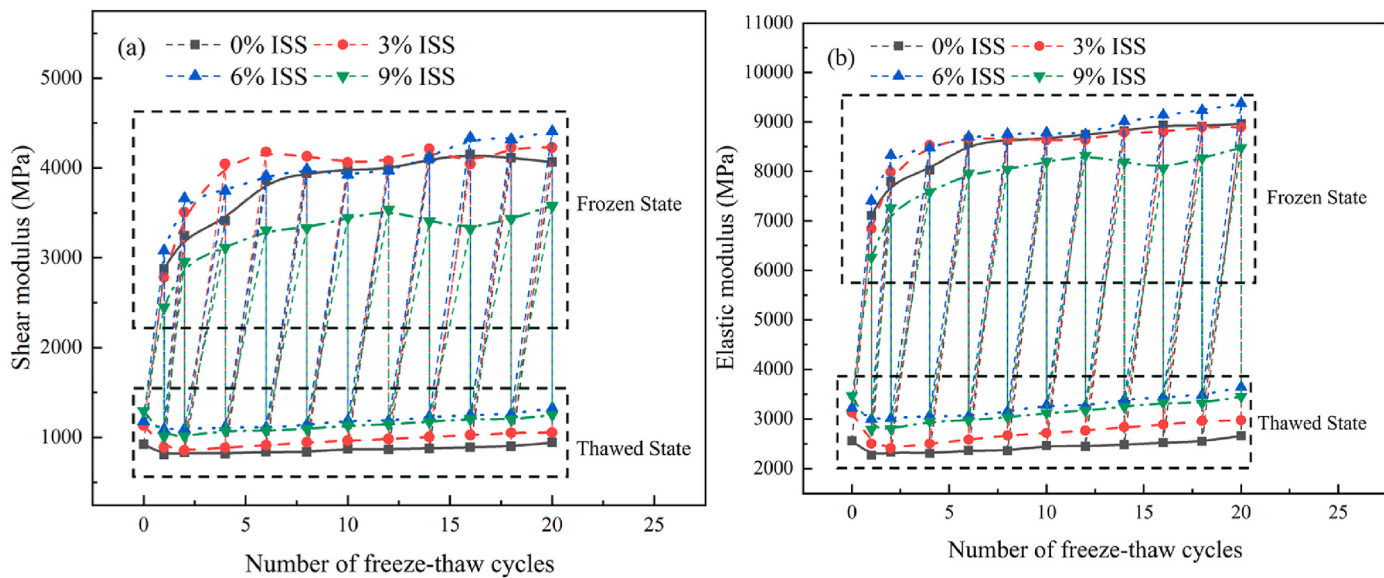


Fig. 3. Mechanical parameters of stabilized soil under frozen and thawed state: (a) shear modulus (G_0), (b) elastic modulus (E_0).

3. Results

3.1. Elastic wave velocity

The elastic wave signals and the corresponding S- and P-wave velocities are presented in Fig. 2. To illustrate typical waveform responses, 0 % ISS and 9 % ISS specimens were selected as examples. Fig. 2(a)–(d) show the S-wave and P-wave signals of these two specimens during the freeze-thaw cycles. Specifically, panels (a) and (b) present the S-wave signals of the 0 % and 9 % ISS specimens, while (c) and (d) display their corresponding P-wave signals. In these figures, “OT” refers to the condition before freeze-thaw cycling, whereas “1F” and “1T” represent the frozen and fully thawed states during the first cycle, respectively. First arrival points are marked with small circles. Fig. 2(e) and (f) summarize the variations in S-wave and P-wave velocities, respectively, for specimens stabilized with different ISS contents (0 % ISS, 3 % ISS, 6 % ISS, and 9 % ISS) throughout the freeze-thaw process.

As shown in Fig. 2(a) and (b), the first arrival time of S-waves is noticeably shorter for both ISS-treated specimens and that stabilized without ISS in the frozen state. According to Eq. (3), this implies that the S-wave velocity in the frozen state exceeds that in the thawed state. Moreover, the minimal variation in travel time throughout the freeze-thaw cycles indicates that wave velocity remains highly consistent. Only slight changes are observed within 0.018 ms during the initial cycles, indicating that the stabilized specimens exhibit strong resistance to freeze-thaw conditions.

Fig. 2(c) and (d) presents the P-wave signals in both thawed and frozen states. It can be observed that the first arrival time of the P-wave signals is earlier in the frozen state and precedes the first arrival time of the S-wave, indicating that P-waves propagate through the stabilized soil specimens faster than S-waves. Similar to S-waves, the first arrival time of P-waves becomes increasingly stable as the number of freeze-thaw cycles increases. Additionally, the travel times of signals for the 0 % ISS and 9 % ISS specimens show no significant difference, highlighting the need for further analysis based on the calculated wave velocities.

Fig. 2(e), (f) illustrates the variations in S- and P-wave velocities during freeze-thaw cycles, calculated using Eq. (3). As shown in Fig. 2(e), the S-wave velocity of specimens in the thawed state initially decreases during the early freeze-thaw cycles and then gradually increases. The thawed S-wave velocity ranges from 659 to 856 m/s, with the velocities of the 6 % ISS and 9 % ISS specimens being closely aligned, the 3

% ISS specimen slightly lower, and the 0 % ISS specimen the lowest. Notably, ISS-treated specimens exhibit a more pronounced initial reduction in S-wave velocity compared to the untreated 0 % ISS specimen during the early freeze-thaw cycles. In the frozen state, the S-wave velocity shows a continuous increase, with a more rapid rise during the initial cycles. The frozen S-wave velocity ranges from 1177 to 1524 m/s, significantly higher than that in the thawed state. This trend aligns with previous research findings (Kang and Lee, 2015; Park et al., 2021; Park and Lee, 2014).

From Fig. 2(f), it can be observed that the P-wave velocity of the 0 % ISS specimen in the thawed state generally increases over the freeze-thaw cycles. In the early stages, ISS-treated specimens exhibit a slight initial decrease in P-wave velocity. For the thawed state, the P-wave velocity ranges from 1633 to 1838 m/s for 0 % ISS specimens, 1702–1871 m/s for 6 % ISS specimens, 1749–1928 m/s for 3 % ISS specimens, and 1675–1850 m/s for 9 % ISS specimens. The order of P-wave velocity magnitudes is 3 % ISS > 6 % ISS > 9 % ISS > 0 % ISS. In the frozen state, all specimens show a rapid increase in P-wave velocity during the initial freeze-thaw cycles, followed by a gradual rise with additional cycles. The P-wave velocity for all specimens in the frozen state ranges between 2064 and 2238 m/s. Unlike the thawed state, no consistent ranking of P-wave velocity is observed among the specimens with different ISS contents during freeze-thaw cycles.

3.2. Shear modulus and elastic modulus

The G_0 and E_0 of the stabilized specimens are shown in Fig. 3. Since the specimens were laterally confined and exhibited negligible vertical deformation during testing, and were maintained in a sealed environment, the trends observed in G_0 closely mirror those of the S-wave velocity, as illustrated in Fig. 3(a). Specifically, G_0 decreases initially and then increases in the thawed state, while it exhibits a rapid increase followed by a gradual rise in the frozen state as freeze-thaw cycles progress. In the thawed state, G_0 ranges from 808 to 1325 MPa, whereas in the frozen state, it ranges from 2448 to 4409 MPa. After 20 freeze-thaw cycles, the G_0 values of the 0 % ISS, 3 % ISS, 6 % ISS, and 9 % ISS specimens in the thawed state were 943, 1055, 1325, and 1251 MPa, respectively. The ranking of G_0 is as follows: 6 % ISS > 9 % ISS > 3 % ISS > 0 % ISS, with the values of 6 % ISS and 9 % ISS specimens being very close. Additionally, the growth rate of G_0 for ISS-treated specimens exceeds that of the 0 % ISS specimen.

Fig. 3(b) shows that E_0 exhibits a similar trend to the G_0 during

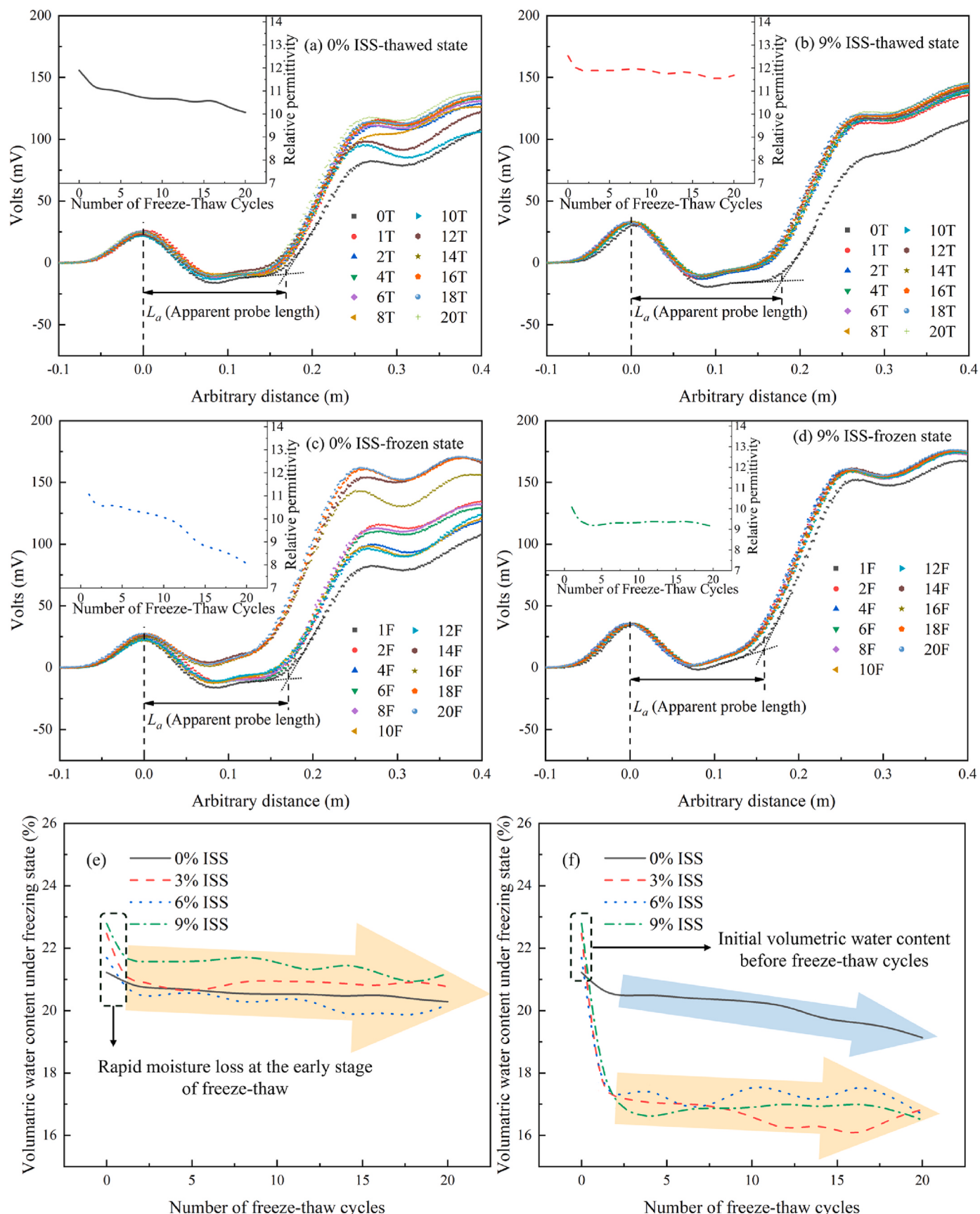


Fig. 4. Waveform of TDR signals under thawing state: (a) 0 % ISS-thawed state, (b) 9 % ISS-thawed state, (c) 0 % ISS-frozen state, (d) 9 % ISS-frozen state, (e) volumetric water content under thawed state (f) volumetric water content under frozen state.

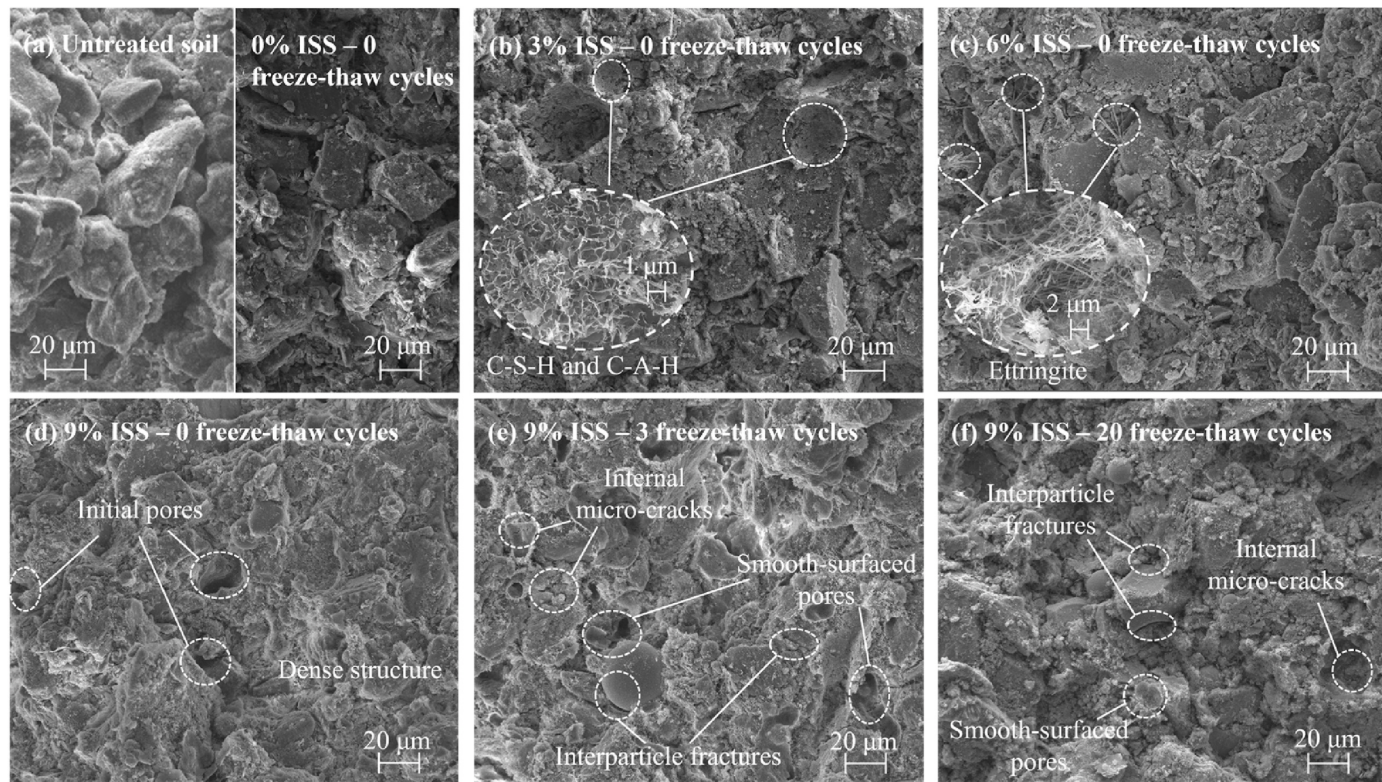


Fig. 5. Scanning electron microscopy images showing microstructural changes in untreated and ISS-stabilized soils: (a) untreated and 0 % ISS specimens before freeze-thaw; (b), (c), (d) specimens with 3 %, 6 %, and 9 % ISS after curing; (e), (f) 9 % ISS specimen after 3 and 20 freeze-thaw cycles.

freeze-thaw cycles. In the thawed state, E_0 ranges from 2269 to 3644 MPa, while in the frozen state, it ranges from 6263 to 9377 MPa. After 20 freeze-thaw cycles, the E_0 values of the 0 % ISS, 3 % ISS, 6 % ISS, and 9 % ISS specimens in the thawed state were 943, 1055, 1325, and 1251 MPa, respectively. The ranking of E_0 among the specimens is consistent with that of G_0 , with 6 % ISS and 9 % ISS specimens showing comparable values. This indicates that the freeze-thaw resistance of the specimens does not increase linearly with ISS content. Beyond 6 % ISS, G_0 and E_0 of the specimens after freeze-thaw cycles even slightly decrease. Moreover, no linear relationship is observed between ISS content and these parameters in the frozen state. In the later stages of freezing, the G_0 and E_0 of 0 % ISS, 3 % ISS, and 6 % ISS specimens converge, while the 9 % ISS specimen shows the lowest values. Notably, ISS-treated specimens exhibit a faster growth rate in G_0 and E_0 during the initial freeze-thaw cycles.

3.3. Volumetric water content

The TDR signals of the 0 % and 9 % ISS specimens in thawed and frozen states are shown in Fig. 4. Subfigures (a)–(d) correspond to the thawed 0 % ISS, thawed 9 % ISS, frozen 0 % ISS, and frozen 9 % ISS specimens, respectively. The volumetric water content during freeze-thaw cycles, estimated from the calibrated relation between relative permittivity and water content, is presented in Fig. 4(e) and (f).

From Fig. 4(a) and (b), it can be observed that the TDR signal of the 0 % ISS specimen in the thawed state shows minimal variation, with the relative permittivity, calculated using Eq. (1), gradually decreasing at a slow rate. In contrast, the signal of the 9 % ISS specimen in the thawed state exhibits a sudden shift during the early freeze-thaw cycles but subsequently stabilizes and overlaps. The relative permittivity for the 9 % ISS specimen initially decreases sharply in the early stages but decreases more gradually during later cycles. In Fig. 4(c) and (d), the TDR signal of the 0 % ISS specimen in the frozen state shifts upward slowly during freeze-thaw cycles, and the L_a value decreases gradually.

Correspondingly, the relative permittivity decreases progressively with the number of cycles. For the 9 % ISS specimen in the frozen state, the signal shows a sudden shift in the early freeze-thaw cycles but stabilizes and overlaps in subsequent cycles. The relative permittivity for the 9 % ISS specimen decreases sharply in the early stages but remains nearly constant in later cycles.

As shown in Fig. 4(e), under the thawed state, all specimens experienced a decrease in volumetric water content after the first freeze-thaw cycle, with the reduction being the smallest for the 0 % ISS specimen. Following the initial freeze-thaw cycle, the volumetric water content of all specimens exhibited a gradual downward trend. Fig. 4(f) shows the volumetric water content in the frozen state, representing the unfrozen water content. When the freeze-thaw cycle count is 0, the volumetric water content corresponds to the initial value before freezing. In the frozen state, the volumetric water content of the 0 % ISS specimen exhibited only a slight decrease, whereas specimens with ISS showed a significant reduction, particularly during the initial freeze-thaw cycles, indicating that more water underwent phase transition to ice compared to the 0 % ISS specimen.

A comparison of Fig. 4(e) and (f) reveals that the volumetric water content of the 0 % ISS specimen decreased more rapidly in the frozen state than in the thawed state. In the thawed state, water reduction was primarily due to chemical reactions, whereas in the frozen state, the reduction resulted from a combination of chemical reactions and water phase transitions. The faster reduction in water content in the frozen state compared to the thawed state indicates that the amount of water undergoing phase transition increased with additional cycles. For ISS-treated specimens, the frozen state showed no significant reduction in volumetric water content, suggesting that although more water underwent phase transition initially, the structure of the ISS-treated specimens became steadier than 0 % ISS specimen after multiple freeze-thaw cycles, preventing further increases in phase transition-related water loss.

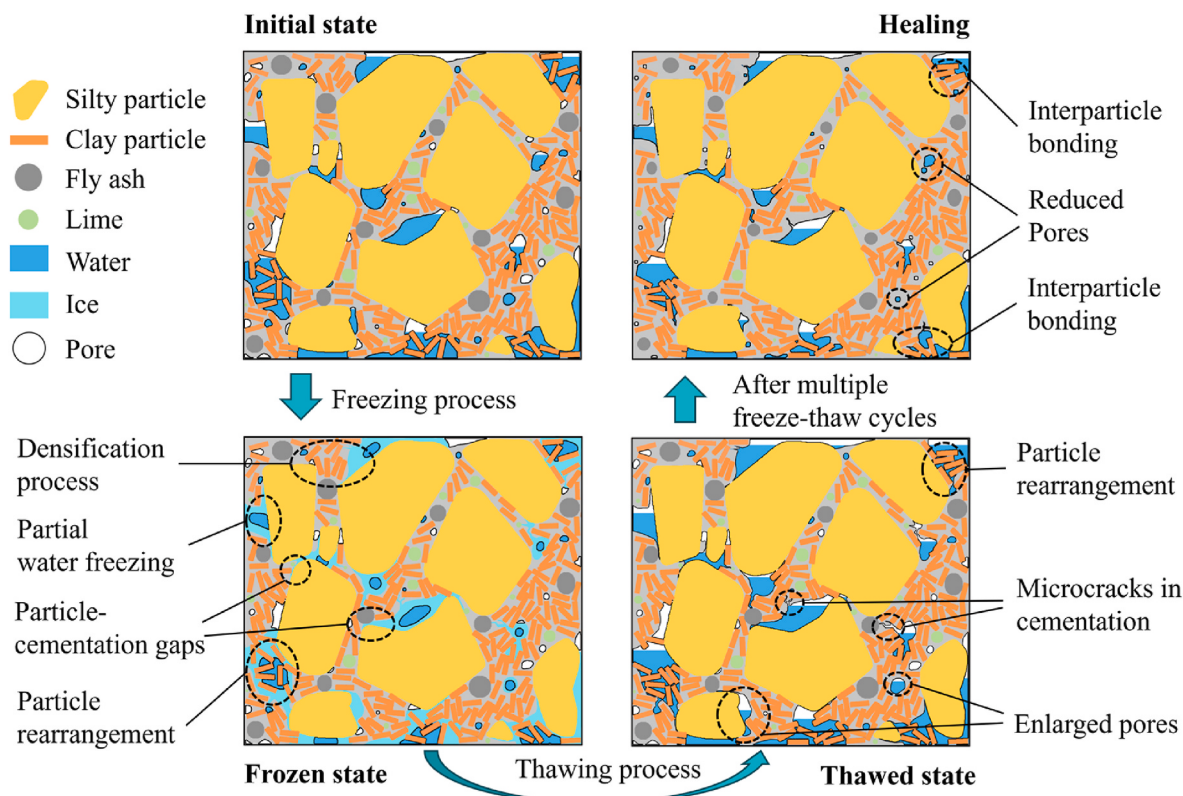


Fig. 6. Mechanism diagram of freeze-thaw effects on stabilized specimens.

3.4. Microstructural analysis

Fig. 5 presents scanning electron microscopy images of untreated soil (without stabilization or curing), as well as 0 % ISS, 3 % ISS, 6 % ISS, and 9 % ISS specimens after curing but before freeze-thaw exposure. Additionally, microstructures of the 9 % ISS specimen after 3 and 20 freeze-thaw cycles are shown. As shown in Fig. 5(a), the untreated soil exhibits large pores and loose particle contacts, whereas the 0 % ISS specimen displays smaller interparticle pores and improved structural integrity. With the addition of ISS, the structure becomes denser than 0 % ISS specimen, as observed in Fig. 5(b)–(d). Cementitious products, primarily calcium silicate hydrate (C-S-H) and calcium aluminate hydrate (C-A-H), are clearly observed within the matrix, effectively filling pores and enhancing interparticle bonding. Ettringite, although present, mainly contributes to microstructural void filling rather than bonding.

The microstructural evolution during freeze-thaw cycles is illustrated using the 9 % ISS specimens in Fig. 5(d)–(f). Prior to freeze-thaw cycles, the soil matrix appears dense with few visible pores. After three cycles, distinct interparticle fractures between cementitious products and soil particles, along with internal micro-cracks within the cementitious matrix, become evident, consistent with previous studies on freeze-thaw induced degradation of cementitious materials (Yang et al., 2024). However, no significant particle breakage was observed, which contrasts with typical behavior reported for untreated soils subjected to freeze-thaw conditions (S. Zhang et al., 2023). In addition, smooth-surfaced pores surrounded by cementitious products were noted. After 20 freeze-thaw cycles (Fig. 5(f)), the overall structure shows enhanced integrity, with diminished interparticle fractures and fewer micro-cracks and smooth-surfaced pores, indicating a recovery effect within the soil matrix.

4. Discussion

4.1. Mechanism analysis of freeze-thaw cycles

As shown in the wave velocity analysis, both the G_0 and E_0 of the specimens in the frozen state are significantly higher than those in the thawed state. This difference is primarily attributed to the phase transition of water into ice, which fills the pore spaces between soil particles and acts as a bonding agent, thereby enhancing the structural integrity and stiffness of soil. However, the freezing process also introduces internal damage (Shi et al., 2025; Yan et al., 2024a, 2024b). The volumetric expansion associated with water phase change intrudes into the interfaces between soil particles and cementitious products, resulting in the formation of distinct interparticle fractures and internal micro-cracks within the cementitious matrix (Fig. 5(e)). Additionally, the newly formed C-S-H and C-A-H gels are initially porous and loosely structured (Allen et al., 2007; Richardson, 2008). These hydration products are compressed by ice-induced expansion, and upon thawing, smooth-surfaced pores are observed (Fig. 5(e)). The combined effects of micro-cracks, interfacial fractures, and smooth-walled pores compromise the overall integrity of the soil structure, leading to a notable reduction in G_0 and E_0 during the thawed state in the early freeze-thaw cycles (Fig. 3).

These structural degradations are accompanied by changes in water content. As analyzed in Section 3.3, the volumetric water content decreased gradually after the first freeze-thaw cycle. Since the specimens were sealed, this reduction cannot be explained by external moisture loss but rather indicates ongoing chemical reactions between the stabilizer and soil. On one hand, pozzolanic reactions responsible for generating cementitious products typically progress slowly and require extended durations to reach completion. Even after 24 h of accelerated curing, these reactions remain incomplete and continue over time (Nan et al., 2025). On the other hand, the partial disruption of cementation bonds due to freeze-thaw action increases the specific surface area and

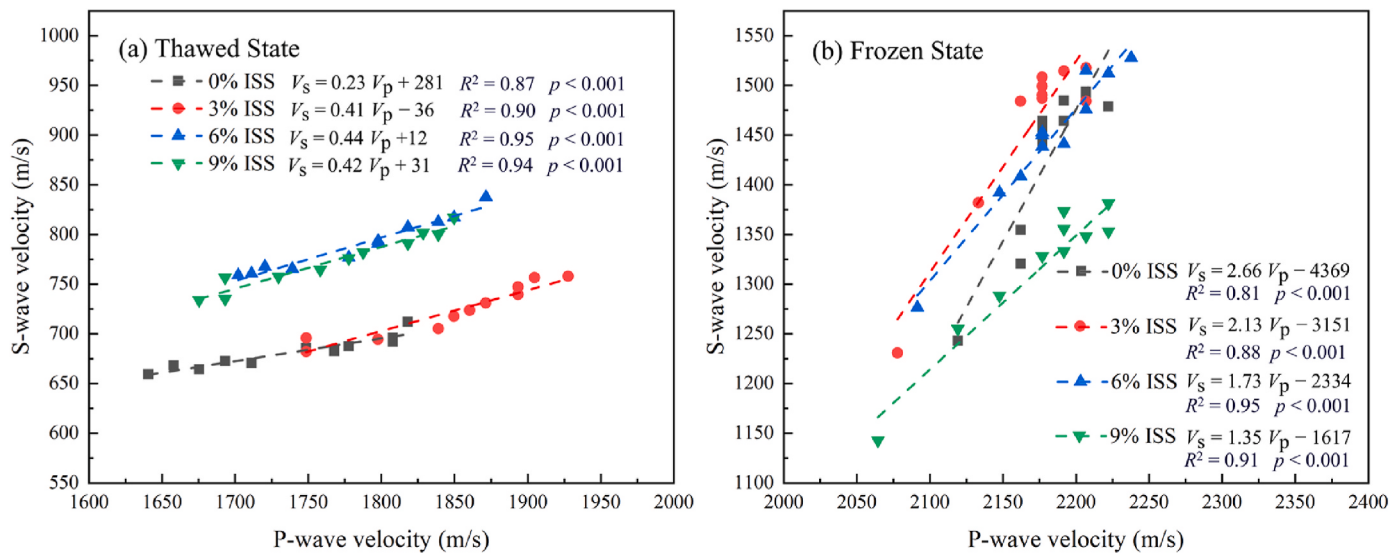


Fig. 7. The relationship between P- and S-wave velocity: (a) thawed state, (b) frozen state.

exposes new reactive sites (Kong et al., 2022; Nan et al., 2024), thereby enhancing chemical interactions during the thawing phase. Consequently, pozzolanic reactions between lime and fly ash are accelerated, leading to continued formation of C-S-H and C-A-H gels. These hydration products fill pre-existing pores and heal freeze-thaw induced cracks, thereby contributing to long-term stabilization and structural recovery.

As the freeze-thaw cycles progress, the self-healing effects of ongoing pozzolanic reactions gradually surpass the damage caused by freezing. During this stage, the rate of moisture reduction slows down (Fig. 4), and the values of G_0 and E_0 in the thawed specimens begin to increase, indicating enhanced stiffness and structural integrity. This trend is further supported by Fig. 5(f), which shows improved continuity and bonding within the microstructure after 20 freeze-thaw cycles. These observations align with previous findings that soil structures tend to stabilize following initial freeze-thaw damage (Ng et al., 2022; Shiba and Kamei, 2014). In some cases, such as soils stabilized with polyvinyl alcohol and quicklime, strength was even reported to slightly increase after 20 cycles, attributed to structural densification and healing effects following early-stage damage (Krainiukov et al., 2020; Nan et al., 2022).

Based on the results and discussion above, the microscopic mechanism of ISS-lime-fly ash stabilized soil during freeze-thaw cycles can be illustrated as shown in Fig. 6. In the initial stage, a well-developed cementation structure is already present. When the temperature drops to -5°C , part of the water within the soil freezes and undergoes volumetric expansion, compressing and rearranging the surrounding cementitious materials and clay particles. Additionally, some ice infiltrates the gaps between cementitious materials and soil particles, as well as the pores within relatively loose cementitious structures. Under these conditions, the ice bonds soil particles and fills pores, resulting in a significant increase in both S- and P-wave velocities. After thawing, the soil structure exhibits increased porosity compared to its initial state. Particle-cementation gaps form between particles and cementitious materials, and micro-cracks develop within the cementitious products, leading to a reduction in the overall structural integrity of the soil. As freeze-thaw cycles advance, additional cementitious products form, gradually repairing the particle-cementation gaps created during the initial cycles. New interparticle bonds develop, while pores are effectively filled, thereby enhancing the overall structural integrity of the soil.

4.2. Differences in freeze-thaw behavior with varying ISS contents

The primary mechanism of ISS is to reduce the thickness of the water

film on soil particle surfaces, thereby releasing more free water (Al-Dakheeli et al., 2021). This promotes phase transitions at subzero temperatures, leading to a greater reduction in unfrozen water content in ISS-treated specimens compared to the 0 % ISS specimen during the freezing stage (Fig. 4(f)). The resulting increase in ice formation induces volumetric expansion and associated stress, which may disrupt the stabilized soil structure. This explains the faster decreases in G_0 and E_0 observed in the thawed state during the early freeze-thaw cycles.

To further investigate the effects of ISS content on the behavior of stabilized soils during freeze-thaw cycles, the relationship between S- and P-wave velocities in both thawed and frozen states is presented in Fig. 7. The relationship can be fitted using linear equations, consistent with findings from previous studies (Oloruntobi et al., 2019; Omovie and Castagna, 2020). The slope of the fitted line reflects the sensitivity of wave velocities to microstructural changes during freeze-thaw cycles. A slope greater than 1.00 indicates that S-wave velocity is more sensitive to structural changes than P-wave velocity, whereas a slope less than 1.00 suggests that P-wave velocity is more sensitive.

As shown in Fig. 7(a), the slope of the fitted equation in the thawed state is less than 1.00, indicating that P-wave velocity is more sensitive to structural changes of soil. Previous research suggests that the formation of cementitious bonds significantly enhances S-wave velocity, whereas its impact on P-wave velocity is relatively minor (Han, 1994). The increase in P-wave velocity is mainly governed by soil porosity, with velocity rising as the pores are filled (Lee and Yoon, 2014). In the thawed state, the increase in wave velocity is primarily attributed to the reaction between stabilizers and soil particles, which enhances the overall structural strength. Thus, the more sensitive P-wave velocity may be because the cementitious products formed during the initial curing phase have already bonded the soil particles sufficiently, and the products generated during freeze-thaw cycles primarily fill residual pores.

As shown in Fig. 7(b), in the frozen state, the slope is greater than 1.00, suggesting that S-wave velocity increases more significantly than P-wave velocity, reflecting the dominant effect of water-ice phase transition bonding on S-wave velocity. In the thawed state, the slope for ISS-treated specimens is higher than that for 0 % ISS specimens, indicating that ISS more effectively promotes reaction products to bond soil particles during freeze-thaw cycles. However, in the frozen state the slope for 0 % ISS specimens is notably higher than for ISS-treated ones, implying that as freeze-thaw cycles progress, the bonding effect of the water-ice phase transition in 0 % ISS specimens intensifies. This is consistent with the earlier finding that 0 % ISS specimens experience a

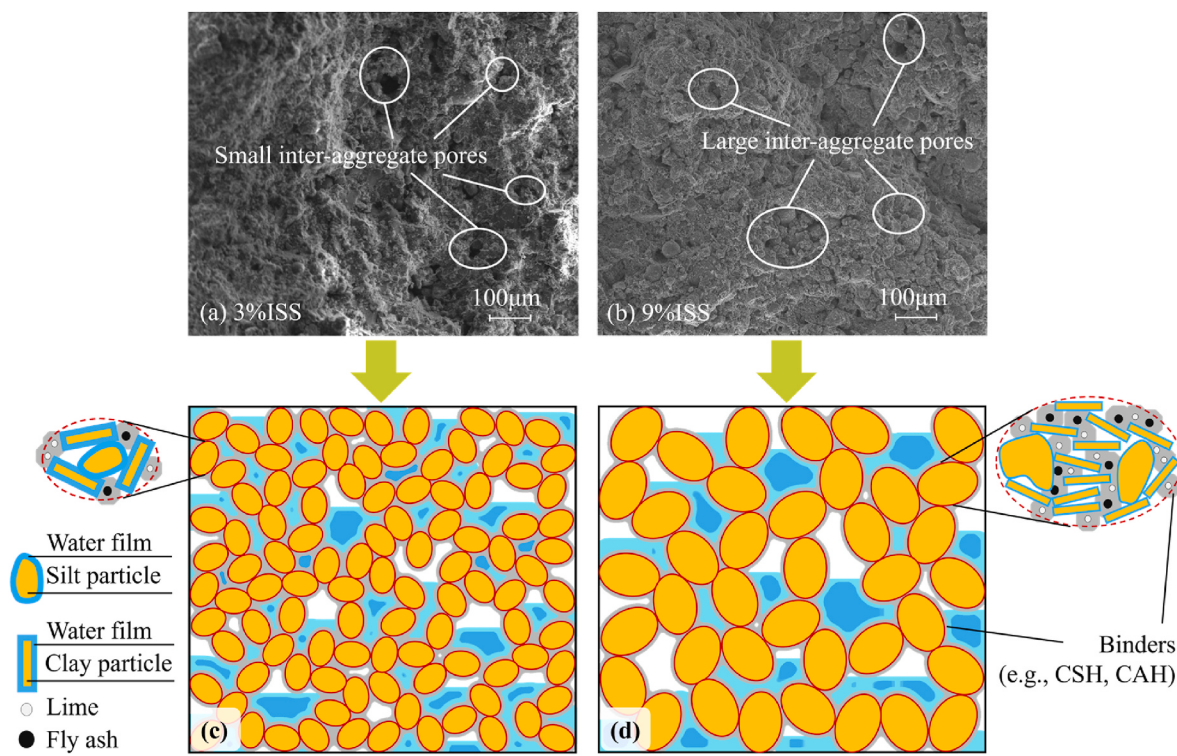


Fig. 8. Structural differences of specimens with varying ISS contents: (a), (b) scanning electron microscopy images and (c), (d) schematic illustrations of specimens with 3 % and 9 % ISS, respectively.

more rapid reduction in unfrozen water content, indicating that it is less stable under freeze-thaw cycles and more pronounced water phase transition and particle bonding. Furthermore, as ISS content increases, the slope gradually decreases while changes in unfrozen water content remain minimal, suggesting that low-ISS specimens tend to form bonds rather than ice-filled pores.

The scanning electron microscopy images of specimens with varying ISS contents prior to curing (Fig. 8(a) and (b)) reveal a significant impact of ISS content on the microstructure of the soil. As the ISS content increases, the pores between soil aggregates become more pronounced (Fig. 8(a) and (b)). This is because ISS reduces the thickness of the water film on the surface of clay particles, facilitating the formation of aggregates (Al-Dakheeli et al., 2021; Jia et al., 2024; Niu et al., 2025; Wu et al., 2021b). Under identical initial density and water content conditions, specimens with low ISS content exhibit smaller pores between aggregates. During freezing, water phase transitions more easily form bonds between aggregates in these specimens (Fig. 8(c)). In contrast, in specimens with high ISS content, the contact between soil particles is tighter, resulting in larger pores between aggregates. During freezing, ice primarily serves to fill these pores rather than forming significant bonds (Fig. 8(d)). This explains why the slope of the S-wave to P-wave velocity fitting line is greater for low-ISS specimens during the freezing stage. Smaller pores in low-ISS specimens promote ice-induced bonding, while in high-ISS specimens, ice mainly contributes to pore filling rather than structural bonding.

5. Summary and conclusion

This study examined the freeze-thaw performance of saline soil stabilized with ISS, lime, and fly ash. A series of non-destructive tests and microstructural analyses were conducted to reveal the evolution of stiffness, unfrozen water content, and pore structure under cyclic freezing and thawing. The main findings are summarized as follows:

(1) ISS-lime-fly ash stabilization significantly enhances soil durability in cold regions. The inclusion of ISS reduces the thickness of water films on particle surfaces, increasing free water availability and promoting ice formation and pozzolanic reactions.

(2) During early freeze-thaw cycles, the thawed-state stiffness (G_0 and E_0) declines due to structural damage, including interparticle fractures and microcracks. However, as cycles progress, continued hydration reactions repair microstructural defects, and stiffness recovers steadily. After 20 cycles, both stiffness and integrity improve, with G_0 and E_0 reaching 1055–1325 MPa and 2973–3644 MPa, respectively.

(3) Microstructural observations confirm the progressive densification of cementitious products, and ISS-lime-fly ash treated specimens demonstrate superior long-term stability compared with lime-fly ash alone, underscoring the potential of ISS as a sustainable additive for enhancing the freeze-thaw resistance of saline soils.

CRediT authorship contribution statement

Jiyun Nan: Writing – original draft, Visualization, Investigation, Formal analysis, Data curation. **Jiankun Liu:** Writing – review & editing, Supervision, Resources, Project administration, Funding acquisition. **Dan Chang:** Writing – review & editing, Supervision, Resources, Project administration, Funding acquisition. **Jong-Sub Lee:** Writing – review & editing, Validation, Supervision, Resources, Project administration, Investigation, Funding acquisition, Conceptualization. **Xue Li:** Writing – review & editing, Visualization, Validation, Methodology, Investigation, Formal analysis, Conceptualization.

Declaration of competing interest

We declare that we have no financial and personal relationships with other people or organizations that can appropriately influence our work, there is no professional or other personal interest of any nature or

kind in any product, service and/or company that could be construed as influencing the position presented in, or the review of, the manuscript entitled.

Acknowledgments

This work was supported by the National Research Foundation of Korea (NRF) grant funded by the Korea government (MSIT) (No. RS-2021-NR060085) and the Natural Science Foundation of China (Nos. 42071078, 42171130, 42201138).

Appendix A. Supplementary data

Supplementary data to this article can be found online at <https://doi.org/10.1016/j.jclepro.2025.146728>.

Data availability

Data will be made available on request.

References

- Al-Dakheeli, H., Arefin, S., Bulut, R., Little, D., 2021. Effectiveness of ionic stabilization in the mitigation of soil volume change behavior. *Transport Geotech* 29, 100573. <https://doi.org/10.1016/j.trgeo.2021.100573>.
- Allen, A.J., Thomas, J.J., Jennings, H.M., 2007. Composition and density of nanoscale calcium-silicate-hydrate in cement. *Nat. Mater.* 6, 311–316. <https://doi.org/10.1038/nmat1871>.
- Amin, M., Agwa, I.S., Mashaan, N., Mahmood, S., Abd-Elrahman, M.H., 2023. Investigation of the physical mechanical properties and durability of sustainable ultra-high performance concrete with recycled waste glass. *Sustainability* 15, 3085. <https://doi.org/10.3390/su15043085>.
- Baker, J.M., Allmaras, R.R., 1990. System for automating and multiplexing soil moisture measurement by time-domain reflectometry. *Soil Sci. Soc. Am. J.* 54, 1–6. <https://doi.org/10.2136/sssaj1990.03615995005400010001x>.
- Cabeza, L.F., Barreneche, C., Miró, L., Morera, J.M., Bartolí, E., Inés Fernández, A., 2013. Low carbon and low embodied energy materials in buildings: a review. *Renew. Sustain. Energy Rev.* 23, 536–542. <https://doi.org/10.1016/j.rser.2013.03.017>.
- Chen, C., Zhang, C., Liu, X., Pan, X., Pan, Y., Jia, P., 2023. Effects of freeze-thaw cycles on permeability behavior and desiccation cracking of dalian red clay in China considering saline intrusion. *Sustainability* 15, 3858. <https://doi.org/10.3390/su15043858>.
- Chen, K., Huang, S., Liu, Y., Ding, L., 2022. Improving carbonate saline soil in a seasonally frozen region using lime and fly ash. *Geofluids*, 7472284. <https://doi.org/10.1155/2022/7472284>, 2022.
- Davis, J.L., Chudobiak, W.J., 1975. In Situ Meter for Measuring Relative Permittivity of Soils.
- Dong, C., Chen, X., Mu, Y., Duan, Z., Xue, Q., Sun, C., Li, J., 2024. Microscopic analysis of deformation and water-salt transport in chlorine saline soils under unidirectional freezing in cold and arid zones. *J. Rock Mech. Geotech. Eng.* <https://doi.org/10.1016/j.jrmge.2024.02.049>.
- Dwivedi, S.K., Vishwakarma, M., Soni, ProfA., 2018. Advances and researches on non destructive testing: a review. *Mater. Today: Proc.* 7th Int Conf. Mater. Process. Character. 5, 3690–3698. <https://doi.org/10.1016/j.matpr.2017.11.620>. March 17–19, 2017.
- Han, D., 1994. Weak Cementation Effect on Velocities of Sands, vol. 1994. SEG Technical Program Expanded Abstracts, pp. 1069–1072. <https://doi.org/10.1190/1.1822700>.
- Hong, W.-T., Jung, Y.-S., Kang, S., Lee, J.-S., 2016. Estimation of soil-water characteristic curves in multiple-cycles using Membrane and TDR system. *Materials* 9, 1019. <https://doi.org/10.3390/ma9121019>.
- Jia, J., Lu, X., Zhu, J., Wang, J., Zhang, L., Cheng, X., 2024. Effect of ionic soil stabilizer on the properties of lime and fly ash stabilized iron tailings as pavement base. *Constr. Build. Mater.* 450, 138558. <https://doi.org/10.1016/j.conbuildmat.2024.138558>.
- Kakasor Ismael Jaf, D., Ismael Abdulrahman, P., Salih Mohammed, A., Kurda, R., Qaidi, S.M.A., Asteris, P.G., 2023. Machine learning techniques and multi-scale models to evaluate the impact of silicon dioxide (SiO_2) and calcium oxide (CaO) in fly ash on the compressive strength of green concrete. *Constr. Build. Mater.* 400, 132604. <https://doi.org/10.1016/j.conbuildmat.2023.132604>.
- Kang, M., Lee, J.-S., 2015. Evaluation of the freezing-thawing effect in sand-silt mixtures using elastic waves and electrical resistivity. *Cold Reg. Sci. Technol.* 113, 1–11. <https://doi.org/10.1016/j.coldregions.2015.02.004>.
- Karami, H., Pooni, J., Robert, D., Costa, S., Li, Jie, Setunge, Sujeeva, 2021. Use of secondary additives in fly ash based soil stabilization for soft subgrades. *Transport Geotech* 29, 100585. <https://doi.org/10.1016/j.trgeo.2021.100585>.
- Kim, S.Y., Kim, Y., Lee, J.-S., 2021. Effects of frozen water content and silt fraction on unconfined compressive behavior of fill materials. *Constr. Build. Mater.* 266, 120912. <https://doi.org/10.1016/j.conbuildmat.2020.120912>.
- Kong, F., Nie, L., Xu, Y., Rui, X., He, Y., Zhang, T., Wang, Y., Du, C., Bao, C., 2022. Effects of freeze-thaw cycles on the erodibility and microstructure of soda-saline loessal soil in Northeastern China. *Catena* 209, 105812. <https://doi.org/10.1016/j.catena.2021.105812>.
- Krainiukov, A., Liu, J., Kravchenko, E., Chang, D., 2020. Performance of silty sand reinforced with aqueous solution of polyvinyl alcohol subjected to freeze-thaw cycles. *Cold Reg. Sci. Technol.* 174, 103054. <https://doi.org/10.1016/j.coldregions.2020.103054>.
- Kumar, S., Mahto, D., 2013. Recent Trends in Industrial and Other Engineering Applications of Non Destructive Testing: A Review.
- Le Runigo, B., Cuisinier, O., Cui, Y.-J., Ferber, V., Deneele, D., 2009. Impact of initial state on the fabric and permeability of a lime-treated silt under long-term leaching. *Can. Geotech. J.* 46, 1243–1257. <https://doi.org/10.1139/T09-061>.
- Lee, J.-S., Park, G., Byun, Y.-H., Lee, C., 2020a. Modified fixed wall Oedometer when considering stress dependence of elastic wave velocities. *Sensors* 20, 6291. <https://doi.org/10.3390/s2016291>.
- Lee, J.-S., Santamarina, J.C., 2005. Bender elements: performance and signal Interpretation. *J. Geotech. Geoenviron. Eng.* 131, 1063–1070. [https://doi.org/10.1061/\(ASCE\)1090-0241\(2005\)131:9\(1063\)](https://doi.org/10.1061/(ASCE)1090-0241(2005)131:9(1063).
- Lee, J.-S., Yoon, H.-K., 2014. Porosity estimation based on seismic wave velocity at shallow depths. *J. Appl. Geophys.* 105, 185–190. <https://doi.org/10.1016/j.jappgeo.2014.03.018>.
- Lee, J.-S., Yu, J.-D., Han, K., Kim, S.Y., 2020b. Strength characteristics of sand-silt mixtures subjected to cyclic freezing-thawing-repetitive loading. *Sensors* 20, 5381. <https://doi.org/10.3390/s20185381>.
- Lei, J., Liu, W., Chen, X., Wu, J., 2023. Experimental study on ionic soil stabilizer combined with vacuum preloading to solidify sludge. *Bull. Eng. Geol. Environ.* 82, 370. <https://doi.org/10.1007/s10064-023-03394-y>.
- Leong, E., Yeo, S., Rahardjo, H., 2005. Measuring shear wave velocity using bender elements. *Geotech. Test. J.* 28, 488–498. <https://doi.org/10.1520/GTJ12196>.
- Linneman, D.C., Strickland, C.E., Mangel, A.R., 2021. Compressional wave velocity and effective stress in unsaturated soil: potential application for monitoring moisture conditions in vadose zone sediments. *Vadose Zone J.* 20, e20143. <https://doi.org/10.1002/vzj2.20143>.
- Li, Y., Wang, Q., Liu, S., ShangGuan, Y., Fu, H., Ma, B., Chen, H., Yuan, X., 2019. Experimental investigation of the geotechnical properties and microstructure of lime-stabilized saline soils under freeze-thaw cycling. *Cold Reg. Sci. Technol.* 161, 32–42. <https://doi.org/10.1016/j.coldregions.2019.03.003>.
- Ma, F., Wu, B., Zhang, Q., Cui, D., Liu, Q., Peng, C., Li, F., Gu, Q., 2018. An innovative method for the solidification/stabilization of PAHs-contaminated soil using sulfonated oil. *J. Hazard Mater.* 344, 742–748. <https://doi.org/10.1016/j.jhazmat.2017.11.015>.
- Nan, J., Chang, D., Liu, J., Chen, H., Lee, J.-S., Kim, S.Y., 2024. Investigation on the microstructural characteristics of lime-stabilized soil after freeze-thaw cycles. *Transport Geotech* 44, 101175. <https://doi.org/10.1016/j.trgeo.2023.101175>.
- Nan, J., Chang, D., Liu, J., Feng, L., Lee, J.-S., Li, X., 2025. Investigation on the micro-macro properties of ionic soil stabilizer and inorganic materials treated saline soil. *Acta Geotech.* <https://doi.org/10.1007/s11440-025-02721-9>.
- Nan, J., Liu, J., Chang, D., Li, X., 2022. Mechanical characteristics and microstructure study of saline soil stabilized by quicklime after curing and freeze-thaw cycle. *Cold Reg. Sci. Technol.* 201, 103625. <https://doi.org/10.1016/j.coldregions.2022.103625>.
- Ng, C.W.W., Li, Z., Zhang, Q., Zhang, S., Wang, Y., 2022. Effects of soil structure on cyclic freeze-thaw induced volumetric behaviour using a modified double-cell triaxial system. *Cold Reg. Sci. Technol.* 203, 103648. <https://doi.org/10.1016/j.coldregions.2022.103648>.
- Niu, W., Guo, B., Li, K., Ren, Z., Zheng, Y., Liu, J., Lin, H., Men, X., 2024. Cementitious material based stabilization of soft soils by stabilizer: Feasibility and durability assessment. *Constr. Build. Mater.* 425, 136046. <https://doi.org/10.1016/j.conbuildmat.2024.136046>.
- Niu, W., Zheng, Y.-Y., Yin, Z.-Y., Yao, C., Wei, P., 2025. Multiscale mechanical behavior of hydrated expansive soil: insights from experimental and MD study. *Comput. Geotech.* 181, 107129. <https://doi.org/10.1016/j.compgeo.2025.107129>.
- Noborio, K., 2001. Measurement of soil water content and electrical conductivity by time domain reflectometry: a review. *Comput. Electron. Agric.* 31, 213–237. [https://doi.org/10.1016/S0168-1699\(00\)00184-8](https://doi.org/10.1016/S0168-1699(00)00184-8).
- Oloruntobi, O., Onalo, D., Adedigba, S., James, L., Chunduru, R., Butt, S., 2019. Data-driven shear wave velocity prediction model for siliciclastic rocks. *J. Petrol. Sci. Eng.* 183, 106293. <https://doi.org/10.1016/j.petrol.2019.106293>.
- Omovic, S.J., Castagna, J.P., 2020. Relationships between dynamic elastic moduli in Shale reservoirs. *Energies* 13, 6001. <https://doi.org/10.3390/en13226001>.
- Park, J., Kim, J., 2023. Role of temperature-dependent interfacial tension on shear wave velocity for energy geosystems. *Sensors* 23, 8709. <https://doi.org/10.3390/s23218709>.
- Park, J., Lee, J.-S., Won, J., Kim, J., 2021. Evolution of small strain soil stiffness during freeze-thaw cycle: transition from capillarity to cementation examined using magnetic and piezo crystal sensors. *Sensors* 21, 2992. <https://doi.org/10.3390/s21092992>.
- Park, J.-H., Lee, J.-S., 2014. Characteristics of elastic waves in sand-silt mixtures due to freezing. *Cold Reg. Sci. Technol.* 99, 1–11. <https://doi.org/10.1016/j.coldregions.2013.11.002>.
- Pourakbar, S., Maneshmoaveni, A., Moazami, D., Moretti, L., Yousefi, A., Cristelo, N., 2024. Stabilization of clay soil using alkali-activated sewage sludge. *J. Rock Mech. Geotech. Eng.* <https://doi.org/10.1016/j.jrmge.2024.09.029>.
- Qaidi, S., Najm, H.M., Abed, S.M., Ahmed, H.U., Al Dugaishi, H., Al Lawati, J., Sabri, M. M., Alkhathib, F., Milad, A., 2022. Fly ash-based geopolymers composites: a review of

- the compressive strength and microstructure analysis. Materials 15, 7098. <https://doi.org/10.3390/ma15207098>.
- Richardson, I.G., 2008. The calcium silicate hydrates. Cement Concr. Res. 38, 137–158. <https://doi.org/10.1016/j.cemconres.2007.11.005>. Special Issue — The 12th International Congress on the Chemistry of Cement. Montreal, Canada, July 8–13 2007.
- Roadbond, Inc., 2010. LEED Narrative Generic V6 0710 (Technical Documentation). Roadbond, Inc.
- Sahin, U., Angin, I., Kiziloglu, F.M., 2008. Effect of freezing and thawing processes on some physical properties of saline-sodic soils mixed with sewage sludge or fly ash. Soil Tillage Res. 99, 254–260. <https://doi.org/10.1016/j.still.2008.03.001>.
- Scholen, D.E., 1992. Non-Standard Stabilizers (Report No. FHWA-FLP-92-011). United States Department of Agriculture, Forest Service, Southern Region.
- Shi, X., Yang, P., Geng, X., Fan, S., Tang, Y., Lu, Y., 2025. Investigating static properties and microscopic pore structure characteristics of rubberized cement-soil under freeze-thaw cycles. Constr. Build. Mater. 458, 139524. <https://doi.org/10.1016/j.conbuildmat.2024.139524>.
- Shibi, T., Kamei, T., 2014. Effect of freeze-thaw cycles on the strength and physical properties of cement-stabilised soil containing recycled bassanite and coal ash. Cold Reg. Sci. Technol. 106–107, 36–45. <https://doi.org/10.1016/j.coldregions.2014.06.005>.
- Stipho, A.S., 1989. Some engineering properties of stabilized saline soil. Eng. Geol. 26, 181–197. [https://doi.org/10.1016/0013-7952\(89\)90006-9](https://doi.org/10.1016/0013-7952(89)90006-9).
- Sun, Z., Chen, W.-B., Zhao, R.-D., Shen, P., Yin, J.-H., Chen, Y., 2023. Effect of seawater on solidification/stabilisation treatment of marine soft soil slurry by lime-activated ISSA and GGBS. Eng. Geol. 323, 107216. <https://doi.org/10.1016/j.engeo.2023.107216>.
- Topp, G.C., Davis, J.L., Annan, A.P., 1980. Electromagnetic determination of soil water content: measurements in coaxial transmission lines. Water Resour. Res. 16, 574–582. <https://doi.org/10.1029/WR016i003p00574>.
- Vinson, T.S., 1978. Response of frozen ground to dynamic loading. In: Geotechnical Engineering for Cold Regions. McGraw-Hill Book Co., New York, New York, pp. 405–458.
- Wan, X., Hu, Q., Liao, M., 2017. Salt crystallization in cold sulfate saline soil. Cold Reg. Sci. Technol. 137, 36–47. <https://doi.org/10.1016/j.coldregions.2017.02.007>.
- Wang, F., Li, K., Liu, Y., 2022. Optimal water-cement ratio of cement-stabilized soil. Constr. Build. Mater. 320, 126211. <https://doi.org/10.1016/j.conbuildmat.2021.126211>.
- Wang, F., Xiang, W., Corely, T., Yeh, T.-C.J., Yuan, Y., 2018. The influences of freeze-thaw cycles on the shear strength of expansive soil treated with ionic soil stabilizer. Soil Mech. Found. Eng. 55, 195–200. <https://doi.org/10.1007/s11204-018-9525-1>.
- Wang, X., Li, J., Wang, Xu, Zhang, Y., Jiang, D., Zhao, G., 2022. Study on strength and microstructure of red clay reinforced by F1 ionic soil stabilizer. Appl. Sci. 12, 9831. <https://doi.org/10.3390/app12199831>.
- Wei, P., Yin, Z.-Y., Yao, C., Ren, Z., Zheng, Y.-Y., Ma, W., 2024. Atomistic origin of montmorillonite clay subjected to freeze-thaw hysteresis. J. Rock Mech. Geotech. Eng. <https://doi.org/10.1016/j.jrmge.2024.11.004>.
- Wu, X.-T., Qi, Y., Chen, B., 2021a. Solidification effect and mechanism of ionic soil stabilizer applied on high-water-content clay. Bull. Eng. Geol. Environ. 80, 8583–8595. <https://doi.org/10.1007/s10064-021-02433-w>.
- Wu, X.-T., Sun, J.-S., Qi, Y., Chen, B., 2021b. Pore and compression characteristics of clay solidified by ionic soil stabilizer. Bull. Eng. Geol. Environ. 80, 5003–5019. <https://doi.org/10.1007/s10064-021-02145-1>.
- Xu, X., Zhang, W., Wang, Y., 2022. Measuring and modeling the dielectric constant of soil during freezing and thawing processes: an application on silty clay. Acta Geotech. 17, 3867–3886. <https://doi.org/10.1007/s11440-022-01487-8>.
- Yan, Y., Chang, D., Liu, J., Nan, J., Liu, X., Feng, L., 2024a. Study on the macro-microscopic mechanical properties of saline soil stabilized by ionic agent and inorganic materials in cold regions. Constr. Build. Mater. 442, 137650. <https://doi.org/10.1016/j.conbuildmat.2024.137650>.
- Yan, Y., Chang, D., Liu, J., Xu, A., Feng, L., 2024b. Multiscale mechanical analysis of Frozen Clay: triaxial testing and discrete element modeling. Cold Reg. Sci. Technol. 224, 104250. <https://doi.org/10.1016/j.coldregions.2024.104250>.
- Yang, Z., Mou, X., Ji, H., Liang, Z., Zhang, J., 2024. Effects of freeze-thaw on bank soil mechanical properties and bank stability. Sci. Rep. 14, 9808. <https://doi.org/10.1038/s41598-024-60698-z>.
- Zha, F., Liu, S., Du, Y., Cui, K., 2008. Behavior of expansive soils stabilized with fly ash. Nat. Hazards 47, 509–523. <https://doi.org/10.1007/s11069-008-9236-4>.
- Zhang, F., Yang, Z., Joey, Still, B., Wang, J., Yu, H., Zubbeck, H., Petersen, T., Aleshire, L., 2018. Elastic properties of saline permafrost during thawing by bender elements and bending disks. Cold Reg. Sci. Technol. 146, 60–71. <https://doi.org/10.1016/j.coldregions.2017.11.014>.
- Zhang, J., Lai, Y., Zhang, M., You, Z., Li, S., Bai, R., 2024. Study on the coupling mechanism of water-heat-vapor-salt-mechanics in unsaturated freezing sulfate saline soil. Comput. Geotech. 169, 106232. <https://doi.org/10.1016/j.compgeo.2024.106232>.
- Zhang, S., Xu, X., Dong, X., Lei, H., Sun, X., 2023. Effects of freeze-thaw cycles on the mechanical properties and microstructure of a Dispersed soil. Appl. Sci. 13, 9849. <https://doi.org/10.3390/app13179849>.
- Zhang, S., Zhang, J., Gui, Y., Chen, W., Dai, Z., 2020. Deformation properties of coarse-grained sulfate saline soil under the freeze-thaw-precipitation cycle. Cold Reg. Sci. Technol. 177, 103121. <https://doi.org/10.1016/j.coldregions.2020.103121>.
- Zhang, X., Shu, C., Fujii, M., Wu, Y., Sun, D., Ye, P., Bao, Y., 2023. Numerical and experimental study on water-heat-salt transport patterns in shallow bare soil with varying salt contents under evaporative conditions: a comparative investigation. J. Hydrol. 621, 129564. <https://doi.org/10.1016/j.jhydrol.2023.129564>.